University of Groningen

Structure–property relations of three-dimensional nanoporous template-based graphene foams

Peng, Weixiang; Sun, Kun; Onck, Patrick

Published in:
Extreme Mechanics Letters

DOI:
10.1016/j.eml.2022.101737

IMPORTANT NOTE: You are advised to consult the publisher's version (publisher's PDF) if you wish to cite from it. Please check the document version below.

Document Version
Publisher's PDF, also known as Version of record

Publication date:
2022

Link to publication in University of Groningen/UMCG research database

Citation for published version (APA):
Peng, W., Sun, K., & Onck, P. (2022). Structure–property relations of three-dimensional nanoporous template-based graphene foams. *Extreme Mechanics Letters*, *54*, [101737]. https://doi.org/10.1016/j.eml.2022.101737

Copyright
Other than for strictly personal use, it is not permitted to download or to forward/distribute the text or part of it without the consent of the author(s) and/or copyright holder(s), unless the work is under an open content license (like Creative Commons).

The publication may also be distributed here under the terms of Article 25fa of the Dutch Copyright Act, indicated by the "Taverne" license. More information can be found on the University of Groningen website: https://www.rug.nl/library/open-access/self-archiving-pure/taverne-amendment.

Take-down policy
If you believe that this document breaches copyright please contact us providing details, and we will remove access to the work immediately and investigate your claim.

Downloaded from the University of Groningen/UMCG research database (Pure): http://www.rug.nl/research/portal. For technical reasons the number of authors shown on this cover page is limited to 10 maximum.

Extreme Mechanics Letters 54 (2022) 101737

Contents lists available at ScienceDirect

Extreme Mechanics Letters

journal homepage: www.elsevier.com/locate/eml

Structure–property relations of three-dimensional nanoporous template-based graphene foams

Weixiang Peng [a,b], Kun Sun [a,*], Patrick Onck [b,*]

[a] State Key Laboratory for Mechanical Behavior of Materials, Xi'an Jiaotong University, 710049, Xi'an, China
[b] Zernike Institute for Advanced Materials, University of Groningen, 9700 AB Groningen, The Netherlands

ARTICLE INFO

Article history:
Received 22 January 2022
Received in revised form 4 April 2022
Accepted 7 April 2022
Available online 19 April 2022

Keywords:
Nanoporous graphene foams
Structure–property relations
Mechanical properties
Template-based method

ABSTRACT

Recently, much attention has been directed to 3D graphene structures due to their potential of retaining intrinsic 2D graphene properties, in combination with structural flexibility and tunable porosity. From a theoretical point of view, however, it is challenging to build 3D graphene foam structures that accurately represent experimental topological configurations. Here, we generate open-cell 3D graphene structures that closely reflect template-based manufacturing techniques and investigate their mechanical properties. We use all-atom molecular dynamics simulations to relate the overall stiffness, collapse stress and fracture properties to the underlying graphene microstructure represented by the graphene relative density, template relative density and number of graphene layers. We do so for four different template morphologies: gyroids, regular foam (BCC), random foam and nanoporous gold. The overall mechanical properties as a function of graphene relative density are analyzed in terms of power law relations to probe the microstructural deformation modes. Our results show that the open-cell 3D graphene structures feature bending as the dominant deformation mode, with regular graphene foams having the highest stiffness and strength and random foams the lowest. For gyroids we found that a higher template relative density leads to reduced mechanical properties but improved ductility. A similar trend was observed when the number of graphene layers was increased: enhanced ductility but at the expense of a reduced strength. Interestingly, we found that for low graphene density, the gyroids feature a strong self-stiffening response, leading to improvements in both strength as well as ductility. Our findings can be used as a guideline for the experimental design of innovate and lightweight graphene structures with strongly enhanced mechanical properties.

© 2022 Elsevier Ltd. All rights reserved.

1. Introduction

Graphene [1,2] is a two-dimensional honeycomb lattice formed by sp2-hybridized carbon atoms. It has a wide range of high-quality properties that are suitable for energy-related systems such as photocatalysts, energy storage systems, nanoelectronics systems, and lithium-ion batteries. These properties include giant electron mobility [3,4], extremely high thermal conductivity [5,6], and extraordinary mechanical properties [1,7–9]. However, it is still quite difficult to directly use graphene as a structural material or as a constituent phase [10,11]. This is mainly because the aggregation or restacking of graphene sheets [12,13] significantly complicates the processing of 3D graphene owing to the strong van der Waals forces as a consequence of high surface area, high aspect ratio and interfacial instability of graphene [14,15].

Recently, tremendous efforts have been devoted to the integration of two-dimensional (2D) graphene sheets into three-dimensional (3D) graphene macroscopic structures [16–18], such as aerogels [19,20], sponges [21] and foams [22], which has been considered as an effective approach to overcome the aggregation/restacking of graphene sheets. Moreover, the 3D structures can not only endow the 2D graphene materials with additional microstructural features, such as flexibility, porosity and high internal surface area but they also retain the intrinsic properties of 2D graphene [23]. Thus, 3D graphene structural materials have a great potential for graphene to extend its exceptional 2D properties and specific applications to the macroscale in the fields of energy, environment, sensing and engineering [16,17,19,24,25]. Therefore, it is of great importance to investigate the geometrical structure-function relations of 3D graphene structural materials, exploiting their ultra-light weight [26], negative Poisson's ratio [17,21], outstanding compressibility [19,21] and super-elasticity [18,27].

From an experimental synthesis point-of-view, a division can be made into template-free and template-based approaches. In

* Corresponding authors.
E-mail addresses: sunkun@mail.xjtu.edu.cn (K. Sun), p.r.onck@rug.nl (P. Onck).

https://doi.org/10.1016/j.eml.2022.101737
2352-4316/© 2022 Elsevier Ltd. All rights reserved.

the template-free method, the graphene (or graphene oxide) sheets are randomly dispersed in a solution, in which there is a force balance between van der Waals attraction and electrostatic repulsion between the various sheets. The graphene sheets will interact with each other and cross-link to form a 3D structure subject to a specific thermal treatment. Xu et al. [28] developed a one-step hydrothermal process for the formation of a graphene hydrogel, which shows an excellent mechanical strength. Yan et al. [29] developed a simple chemical-reduction-induced self-assembly method for the preparation of 3D graphene architectures with low densities and high mechanical properties. Multiple cross-linked molecules have also been used to drive the self-assembly to a 3D structure [30]. Template-free methods have several advantages such as low-cost, efficiency and enabling mass production but fail in controlling the pore structure and material quality. On the other hand, template-based methods employ chemical vapor deposition (CVD) techniques, depositing the graphene sheets on the surface of a template. The template is thereafter removed. The resulting 3D graphene has good structural integrity and features precise control of the pore size and number of graphene layers. Cheng et al. [24] reported a template-based CVD method which enables fabrication of 3D foam-like graphene structures with nickel foams as templates. The high quality of the graphene sheets, and the almost perfect connection between them resulted in excellent mechanical properties of the 3D material. Recently, controlled sub−60 nm unit cell sizes of freestanding graphene gyroid structures were fabricated by using a CVD method [31]. Furthermore, Regina et al. [32] produced a freestanding 3D turbostratic graphene architectures with a CVD Ni-based template. This 3D material showed an excellent Young's modulus of 30 MPa, which is one of the highest values recorded for sp^2 carbon in a porous structure. Chen et al. [33] reported on a CVD-grown large-scale ultralight nanoporous graphene material that showed extraordinary tensile strength and ductility.

From a theoretical point-of-view, computer simulations have been performed to investigate the elastic and inelastic mechanical response of various 3D graphene materials. Wang et al. [34] and Pan et al. [35] performed coarse grain molecular dynamics simulations to study the microscopic deformation mechanisms of 3D random graphene structures in the presence and absence of cross-link-driven bonding between the graphene sheets. It was found that these 3D random structures were very similar to the experimental self-assembled structures. Meng et al. [36] combined atomistic simulations and continuum modeling to study the out-of-plane compressive deformation behavior of 3D graphene honeycombs. They analyzed the key structure–property relationships of 3D graphene honeycombs and provided a theoretical framework by which it is possible to predict the deformation response. Zhang et al. [37], Shang et al. [38] and Yi et al. [39] did also study similar graphene-based honeycomb structures. In addition, the mechanical properties of Schwarzites integral graphene structures were studied and provided a systematic understanding of the relation between the topologies of Schwarzites and their mechanical properties [40,41].

As presented above, a considerable amount of theoretical studies have been performed in investigating the mechanical properties of 3D graphene structures. However, the structures used in most of the studies only approximately resemble the experimental graphene foam structures, so that a thorough understanding of the structure–property relations is still lacking. In the present investigation, we will study the mechanical properties of 3D graphene structures by focusing exclusively on structures manufactured by the template-based CVD method using all-atom molecular dynamics simulations. Since the final 3D graphene structures strongly depend on the morphologies of the templates used in the CVD experiments, we selected a set of template morphologies that are characteristic for the range of open-cell structures used in templated-based graphene structures: gyroids, regular and random open-cell foams and nanoporous structures. In addition, to carefully represent the key features of template-based CVD processing, we vary the template relative density, the template surface-to-volume ratio (by varying the template relative density) and the number of deposited graphene layers. For these microstructural variations, we study the stiffness, collapse stress and fracture response as a function of graphene foam relative density.

Methods

Constructing the templates. To simulate 3D graphene structures based on the experimental CVD method, the first step is to build the templates. In this paper, four kinds of porous template models have been investigated as shown in Fig. 1a: (i). Gyroids, (ii). Regular foams, (iii). Random foams and (iv). Nanoporous gold. (i) The gyroid template is generated in the standard way, by placing the atoms at the minimal surface morphology [40,42]. (ii). The open-cell foam templates are generated by the 3D Voronoi method, which accurately captures the foaming process leading to the open-cell foam structure [43,44]. Firstly, the nucleation seeds are distributed in 3D space according to a BCC stacking (see Fig. S1), generating a perfectly ordered, 14-sided Kelvin model, in which each cell consists of 6 squares, 8 hexagons and 36 ligaments to fill the space [43]. To get periodic structures, it is necessary to place the nucleation seeds into a bigger cube as shown in Fig. S1a. Secondly, the Voronoi tessellations are generated based on the nucleation seeds. The 14-sided Kelvin cell can be generated by connecting the vertex points of the polygonal cell as shown in Fig. S1b with blue atoms. Thirdly, as shown in Fig. S1c, the strut geometry of the templates have been set according to the fitting functions of ligament cross sectional area in the experimental aluminum foam samples as reported in the literature [43]. (iii). The random foam templates are generated in a similar way as the regular foam templates. The only difference is the distribution of nucleation seeds which are complete random. (iv). The nanoporous gold template is obtained from a morphological model of an experimental nanoporous gold sample obtained by using nano-tomography on the dealloyed samples, which has been reported in detail in our previous work [45].

Generating the 3D graphene structures. After making the four porous templates, the second step is to generate the graphene layers on the surface of the templates as shown in Fig. 1b. Since the synthesis process for the 3D graphene structures based on the four templates are closely similar to each other, only the gyroid case is chosen to illustrate the procedure. In this paper, two different computational synthesis processes have been shown to get two totally different 3D graphene structures: one continuous graphene layer structure in which one fully connected graphene layer is deposited on the surface of the template, and multiple graphene ribbons structure in which multiple individual graphene sheets are deposited on the template. Both are described below.

For the one continuous graphene layer structures, the template in Fig. 1b (i) is composed of a gyroid colored in orange infiltrated by a random distribution of atoms in blue, see step (1). The template is set as a rigid body in our simulations. A Lennard-Jones (LJ) potential is applied to account for the interaction between the blue atoms using $\varepsilon = 0.02$ meV and $\sigma = 4$ Å. For the interactions between the template (orange) and blue atoms also a LJ potential is used with $\varepsilon = 1$ meV and $\sigma = 4$ Å, which is strong enough to make the blue atoms cover the template surface uniformly assuming an NVT ensemble with a Nose–Hoover thermostat for 10 ps. Periodic boundary conditions are applied in the *X, Y, Z* directions. (2) Then, we choose the first

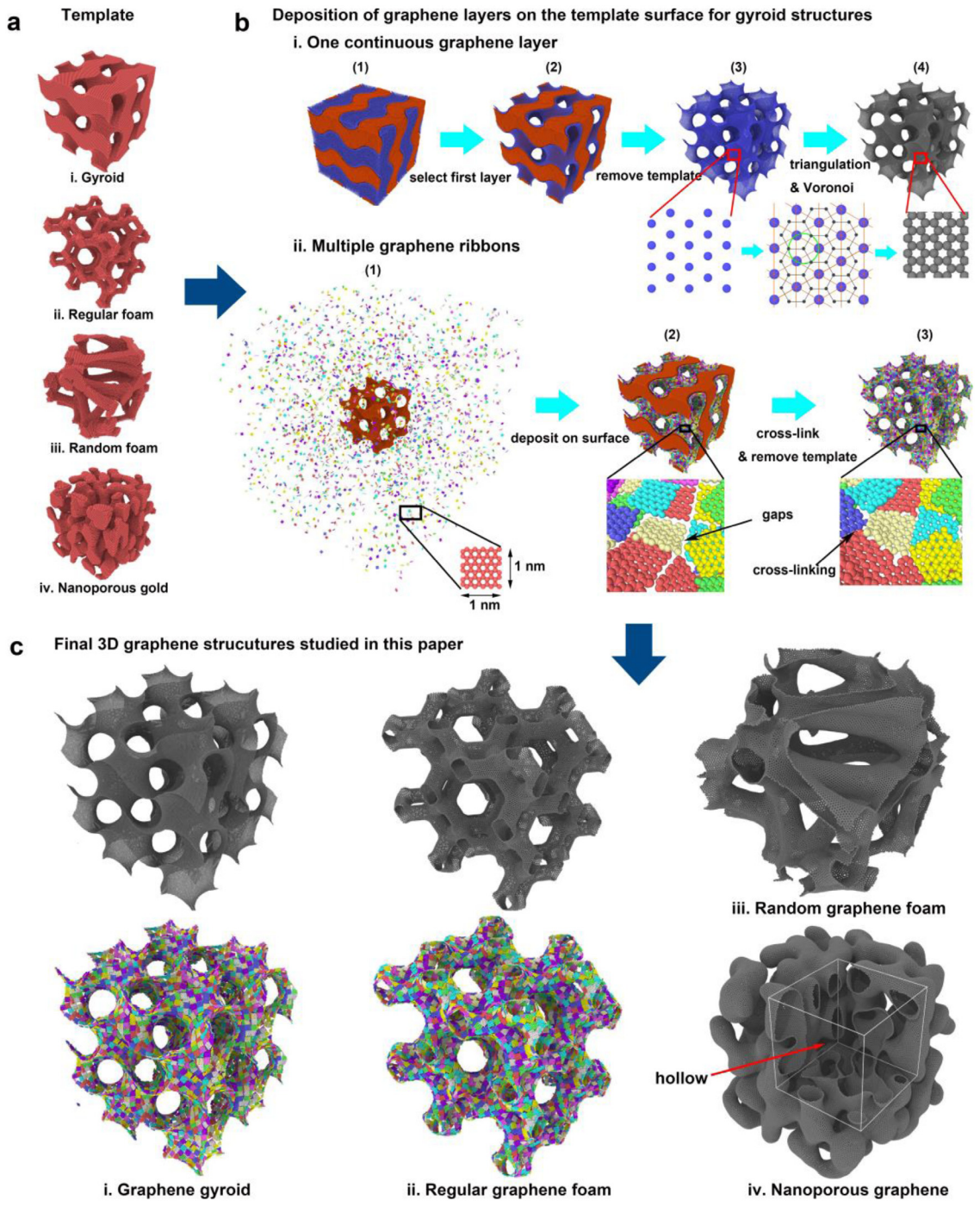

Fig. 1. Schematic diagrams of the 3D graphene structures. (a) Four different templates of porous structures studied in this paper; i. Gyroid; ii. Regular foam; iii. Random foam; iv. Nanoporous gold. (b) Two different computational synthesis methods to grow graphene layers on the surface of the templates (using the gyroid as example); i. One continuous graphene layer, (1) Initial configuration composed of a template with ordered orange atoms and random blue atoms. The random atoms cover the template surface by modifying the attractive force among them. (2) Template coated by a layer of close-packed atoms after selection of the first layer of blue atoms. (3) A single layer of closed-packed (fully triangulated) atoms left after removing the template. (4) One continuous graphene layer is obtained after generating the Voronoi tessellation of the closed-packed triangulated distribution. ii. Multiple graphene ribbons: (1) Initial configuration: a certain amount of graphene ribbons with size 1 nm $\times$ 1 nm distributed randomly in space surrounding and infiltrating a gyroid sample located in the center of the computational domain; (2) Deposit the graphene ribbons on the surface of the template through an attractive potential between graphene ribbons and gyroid surface; (3) Cross-link all the graphene ribbons with each other; then remove the template; (c) Final random 3D graphene structures studied in this paper. i. Graphene gyroid; ii. Regular graphene foam; iii. Random graphene foam; iv. Nanoporous graphene. For i–iv the structures with continuous layers are shown and for i and ii those with multiple graphene ribbons.. (For interpretation of the references to color in this figure legend, the reader is referred to the web version of this article.)

layer of blue atoms, remove the template, and repeat the structure into 27 cubes, as shown in Fig. S1(a). (3) Subsequently, we use these atoms to create a surface triangulation (orange lines) and create a Voronoi tessellation to obtain the graphene structure using black Voronoi nodes. (4) Finally, we cut the central one-unit cube from the 27-cubes (Fig. S1a), representing a 3D graphene unit cell with periodic boundary conditions.

For the gyroids with a coating of multiple graphene ribbons, see Fig. 1b (ii), (1) the initial configurations consist of a collection of graphene ribbons of size 1 nm $\times$ 1 nm distributed randomly

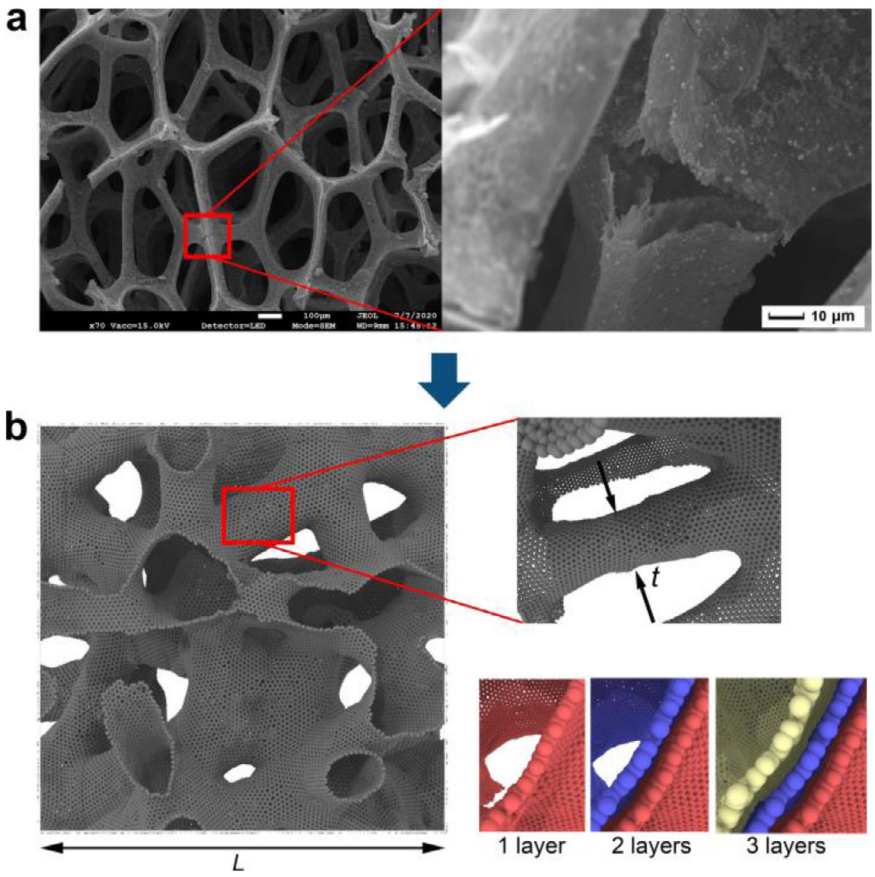

Fig. 2. Parameters of 3D graphene structures studied in this paper. (a) Experimental SEM image of graphene foam based on the CVD method [24]; (b) Random graphene foam of size L (left). Variation of size L for all models: 3.2, 4.7, 6.2, 9.4, 12.2, 14.5, 16.2, 20.2 and 24.4 nm. Different strut thicknesses t: (0.1–0.5) L (top right). Variation of the number of graphene layers: 1, 2 and 3 layers (bottom right).

in space with the template located in its center. The adaptive intermolecular reactive empirical bond order (AIREBO) potential is employed to describe the carbon–carbon interaction within the graphene layer [46]. To avoid a non-physical post-hardening behavior known to occur in the initial AIREBO potential version, the cut-offs are modified to $R_{\min} = R_{\max} = 2.0$ Å [40,47]. Instead of prescribing the true Van der Waals forces between the graphene ribbons through a LJ potential with parameters $\varepsilon = 2.967$ meV and $\sigma = 3.407$ Å, we use the much smaller value $\varepsilon = 0.001$ meV to reduce the attractive forces between the graphene ribbons, which can avoid the intense aggregation of the graphene ribbons. A LJ potential is also used to describe the interaction between the template and graphene ribbons with $\varepsilon = 5$ meV and $\sigma = 3$ Å, resulting in forces between the template and the ribbons that are much bigger than the force between graphene ribbons, which make the graphene ribbons to cover the surface of the template randomly and uniformly. Periodic boundary conditions are applied in the X, Y, Z directions. We assume the structure to be an NPT ensemble with a Nose–Hoover thermostat and a barostat is implemented to control the temperature of the system at 300 K and keep the pressure to be zero in the X, Y, Z direction. As a result, (2) the box will shrink automatically and the graphene ribbons are attracted to the surface of the template. After that, an NVT ensemble with a Nose–Hoover thermostat is assumed and the true Van der Waals forces will be employed for the interaction between the graphene sheets ($\varepsilon = 2.967$ meV). Then, (3) we cross link the graphene sheets by applying the AIREBO potential between all carbon atoms. After that, we remove the template and a 3D structure of crosslinked ribbons remains. All the 3D graphene structures based on gyroid, foam and nanoporous gold templates are shown in Fig. 1c.

Parameters to investigate. The aim of our work is to find the relationship between the mechanical properties and the microstructure of the created 3D graphene structures. The experimental morphology of a graphene foam fabricated by the CVD method [24] is shown in Fig. 2a. To create structures with different relative densities, the size L is varied in the range between 3.2 and 24.4 nm for a fixed atomic spacing. Since the struts are hollow, uniform scaling as done here will create different relative densities of the graphene structures. In addition, also the thickness t of the templates is changed to obtain different relative densities of the 3D graphene structures such as the regular graphene foam of TRD-0.20 and TRD-0.41 in Fig. 9. Different number of layers of 3D graphene sheets has also been taken into consideration to get different densities as used in some experimental studies. All samples of the 3D graphene structures studied in this work are shown in Fig. S2 and S3.

In this paper, molecular dynamics simulations are performed using the large-scale atomic/molecular massively parallel simulator (LAMMPS). The adaptive intermolecular reactive empirical bond order (AIREBO) potential is employed to describe the carbon–carbon interactions within the graphene and the cut-offs are modified to be $R_{\min} = R_{\max} = 2.0$ Å [40,47] as discussed above. Periodic boundary conditions are applied in the X, Y, Z directions for the graphene gyroids and the graphene foams while free boundary conditions are carried out for the non-periodic unit-cell of nanoporous graphene. The simulation time step is 0.001 ps. Before the deformation, the gyroid and foam graphene structures are relaxed by energy minimization, then NPT ensemble conditions with a Nose–Hoover thermostat and barostat are applied to release the stress to zero in the X, Y and Z directions

for 100 ps. For the nanoporous graphene system, NVT ensemble conditions with a Nose–Hoover thermostat and barostat is performed due to the free boundary conditions. The temperature of the system is taken to be 300 K.

In our study, we investigate plane strain as well as plane stress deformation. The former is employed to compare our gyroid results to the existing literature [40,41], while the latter reflects more closely the stress state in uniaxial tension experiments. We used different strain rates (10^{-4} ps^{-1}, 5×10^{-4} ps^{-1},$10^{-3}ps^{-1}$ for the tensile tests and 5×10^{-4} ps^{-1},$10^{-3}ps^{-1}$ and $5 \times 10^{-3}ps^{-1}$ for the compression tests) for our modeling system as shown in Fig. S4. At these rates the effect on the measured properties is small. Considering computational costs, the tensile strain rate is chosen to be 5×10^{-4} ps^{-1} and the compressive strain rate to be $10^{-3}ps^{-1}$, corresponding to values used in similar modeling studies [36,40,48,49].

For the plane stress deformation, the NPT ensemble with Nose–Hoover thermostat and barostat is employed to achieve zero stresses in the directions perpendicular to the tensile direction. For the plane strain deformation, displacements are prescribed in the tensile direction while the displacements in the other two directions are zero. The software Ovito [50] is used to visualize the atomic configurations.

Results and discussion

Computational synthesis of template-based graphene foams. Fig. 1 shows the flow charts of the computational synthesis processes used to obtain the 3D graphene structures in this work. Firstly, four different kinds of solid open-porous materials are selected as templates, including Gyroid, Regular foam, Random Foam and Nanoporous Gold (NPG), since the morphology of the template determines the final morphology of the 3D graphene structures as shown in Fig. 1a. Then, the graphene layers will be generated on the template surface with two different methods: one continuous layer and multiple graphene ribbons as shown in Fig. 1b. The one continuous graphene layer case is a reference case for the experimental template-based CVD technique featuring one fully connected continuous graphene layer. The multiple graphene ribbons case resembles the experimental template-assisted assembly strategy with a fully random distribution of deposited graphene. Finally, six types of 3D graphene structures with different morphology can be generated as described in Fig. 1c. As shown in Fig. 2a and b, the parameters that can experimentally be varied include the sample size L, the strut thickness t and number of graphene layers. Consequently, based on these parameters, we will systematically exploit the relationship between the mechanical properties and the relative density of the 3D graphene structures and find the fundamental influence of these parameters.

Extraction of mechanical properties from stress–strain curves. The uniaxial tension and compressive tests are explored to estimate the mechanical properties of 3D graphene. A typical full stress–strain curve is depicted in Fig. S5. In this work, the Young's modulus E is defined as the slope at zero strain within the strain range from -0.005 to 0.005, we define the maximum stress value as the tensile strength σ_T and the corresponding strain as the tensile strain ε_T. For the compressive strength σ_C, we fit the stress–strain curve in the strain range from -0.4 to 0 by using the equation $\sigma = -\sigma_C [1 - \exp(a\varepsilon)]$, where σ is the compressive stress, ε is the compressive strain, a is a fitting constant value and σ_C is the compressive strength.

Tensile behavior of a graphene gyroid: Effect of template relative density (TRD). We vary the template relative density between 0.10, 0.25 and 0.50 and denote the resulting structures by TRD-0.10, TRD-0.25 and TRD-0.50, respectively. Fig. 3 shows the dependence of Young's modulus E, tensile strength σ_T and tensile strain ε_T on the relative density $\overline{\rho}$. It is clearly demonstrated that the Young's modulus is markedly affected by the morphology of the gyroid structure with a Young's modulus that increases with increasing TRD. As can be seen in Fig. 3d and g, the exponent in the fitting function is closed to 2 (especially for TRD-0.50) for both plane strain and plane stress, which is an indication of a bending-dominated deformation of the graphene walls at the initial elastic stage. The tensile strength σ_T and corresponding tensile strain ε_T, obtained under plane strain and plane stress loading conditions, have been analyzed to get further insight into the mechanical and fracture properties of the different TRD gyroid structures. Here we see a drastically different response for plane strain compared to plane stress, see Fig. 3e, f and h, i. Comparison of Fig. 3e and h shows that σ_T for plane strain follows a regular 1.5 power-law dependence on $\overline{\rho}$, while σ_T for plane stress shows a strong strengthening effect at small $\overline{\rho}$. In addition, for plane strain the failure strain ε_T is independent of density, while for plane stress there is a profound increase in ductility at small $\overline{\rho}$. Together, these results indicate that under plane stress conditions the material features a self-stiffening response, resulting in a drastic increase in tensile strength σ_T and strain ε_T at small densities. The self-stiffening of graphene at low relative densities under plane stress loading conditions has been observed in experiments as well [33]. Here, the difference in morphology due to the different TRD comes in, showing that a large TRD (= 0.50) results in stronger gyroids (see Fig. 3(h) but at the expense of ductility, as clearly shown in Fig. 3i. To investigate this further, we analyze the microstructural evolution for TRD = 0.5 at $\overline{\rho} = 0.05$ in Fig. 4. Here we see that the stress–strain response for plane strain is predominantly linear, while for plane stress there is a profound non-linear stiffening response leading to a larger tensile stress and strain (Fig. 4a and c). This difference can be traced back to the difference in microstructural evolution during straining. Where under plane strain, brittle failure ensues in the absence of lateral contraction (see Fig. 4b), for plane stress, the material is able to laterally contract, leading to a transition from bending to stretching, allowing the material to accommodate the applied strain, and thus postponing the onset of tensile cracking (see Fig. 4d). During this stage, the stress increases linearly with strain initially (until 0.1 strain), but then it undergoes a further increase, reaching a peak at 0.2 strain (see Fig. 4c). This 'self-stiffening' effect is due to the fact that the graphene walls are gradually reorienting towards the tensile direction, which is accommodated by wrinkling and bending of graphene walls in directions transverse to the loading direction (see Fig. 4d). This specific self-stiffening phenomenon has also been demonstrated in previous experimental work [33]. It has been shown that the gradual realignment of the atomic graphene sheets along the tensile direction, where the easily deformed out-of-plane (bending) mode transitions to the strong in-plane (stretching) mode giving rise to self-stiffening and work hardening. These phenomena can be explained by referring to the fundamental anisotropic properties of the graphene ribbons that are extremely strong under in-plane tension but very soft and flexible when subjected to out-of-plane bending. For graphene gyroid TRD=0.5 at a high relative density $\overline{\rho} = 0.18$, the tensile brittle failure under plane strain is similar to the low relative density as shown in Fig. S8a and b while under plane stress the microstructural evolutions of lateral contraction is not too evident as the low relative density case due to the stronger stiffness of higher relative density samples (see Fig. S8c and d).

As can be seen in Fig. 3i for plane stress, the strain ε_T depends on both the relative density $\overline{\rho}$ of graphene and the morphology of the template (i.e., the TRD). A lower TRD has been found to lead to a higher value of ε_T at the peak stress, which is also the case for random graphene structures. To illustrate this effect in more detail, the microstructural evolution of a graphene structure with low TRD (i.e., TRD-0.10) is shown in Fig. 5. Similar to TRD-0.50

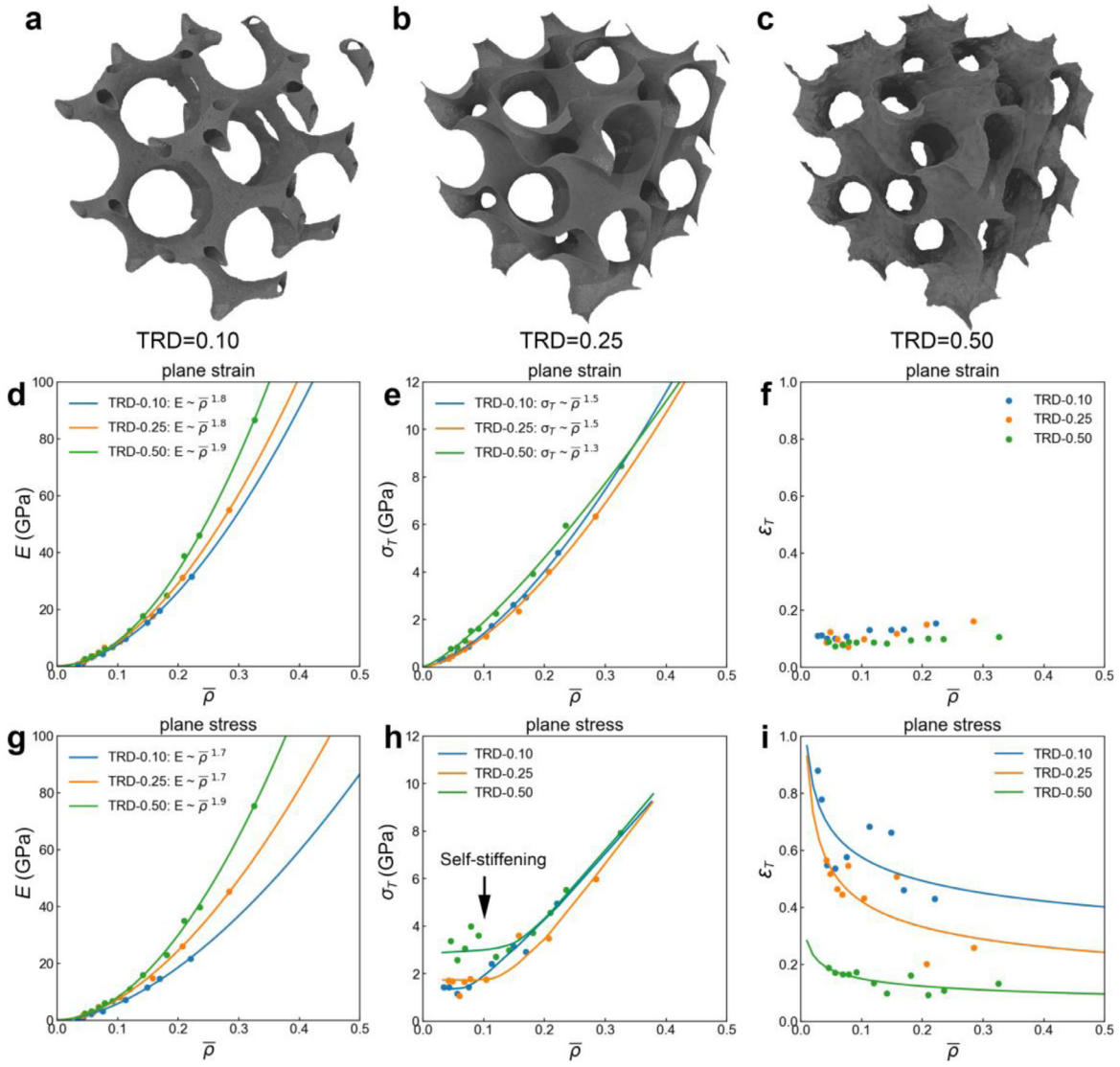

Fig. 3. Effects of TRD on the tensile properties of a graphene gyroid. (a) TRD-0.10, (b) TRD-0.25, and (c) TRD-0.50 graphene gyroid structures. Young's modulus E, tensile strength σ_T, and tensile strain ε_T of graphene gyroid under (d, e, f) plane strain, and (g, h, i) plane stress loading conditions.

(Fig. 4), the deformation process of TRD-0.10 include (i) elastic deformation at small strain, (ii) bending deformation in the lateral x- and y-directions, (iii) stretching deformation in the tensile z-direction at increasing strain, (iv) the initiation and growth of cracks, and (v) final ductile fracture. As shown in the stress–strain curves for TRD-0.10 in Fig. 5d, the main difference between TRD-0.10 and TRD-0.50 is the occurrence of several local peaks prior to the maximum peak. These extra peaks can be directly related to the cracks and their induced microstructural evolution. As can be seen in Fig. 5c and d, crack-1 and crack-2 occur close to the first local peak at a strain value of 0.13. They thereafter expand locally, causing local fracture. The evolutions of these cracks are, in fact, very beneficial for the ductility of the material as they lead to an additional mechanism to accommodate the applied strain resulting in a strong reorientation of the graphene structure in the direction of applied load. Consequently, this accommodation contributes considerably to the very large maximum strain value of approximately 0.66 (see Fig. 3i and Fig. 5c). Finally, crack-3 leads to the final fracture of the graphene structure. At higher relative density the TRD-0.10 structure (see Fig. S9c and d) only shows a minimal local strain accommodation due to the larger stiffness of the structure, resulting in a strong decrease of the tensile strain ε_T and thus a decrease in ductility (see Fig. 3i).

Tensile behavior of a graphene gyroid: Effect of the number of graphene layers. The effect of the number of graphene layers on the Young's modulus of the gyroid structures is depicted in Fig. 6. It clearly shows that the 1-layer gyroid graphene exhibits a much higher Young's modulus than the 2- and 3-layer gyroid structures at the same relative density, indicating that the stacking of the graphene layers reduces the stiffness of the graphene structures per unit mass.

Furthermore, to scrutinize the role of the van der Waals interactions between the different layers on the overall stiffness, we computed the stiffness of the graphene structure, consisting of 3 non-interaction graphene layers, by tripling the corresponding stiffness and density values of the 1-layer graphene, denoted by '(1-layer)×3' in Fig. 6d and g. The results clearly show that by computing the stiffness by loading the three 1-layer structures in parallel, the stiffness per unit density is considerably lower than the 3-layer case, highlighting the role of Van der Waals interactions in stiffening the graphene structures. Also, for the tensile strength σ_T in plane strain and plane stress, the lower number of graphene layers enhances σ_T per unit density. Similar to the previous section, the low-density plane stress cases show self-stiffening (see Fig. 6h) which is absent for plane strain. Self-stiffening occurs at the same slope with relative density, and only

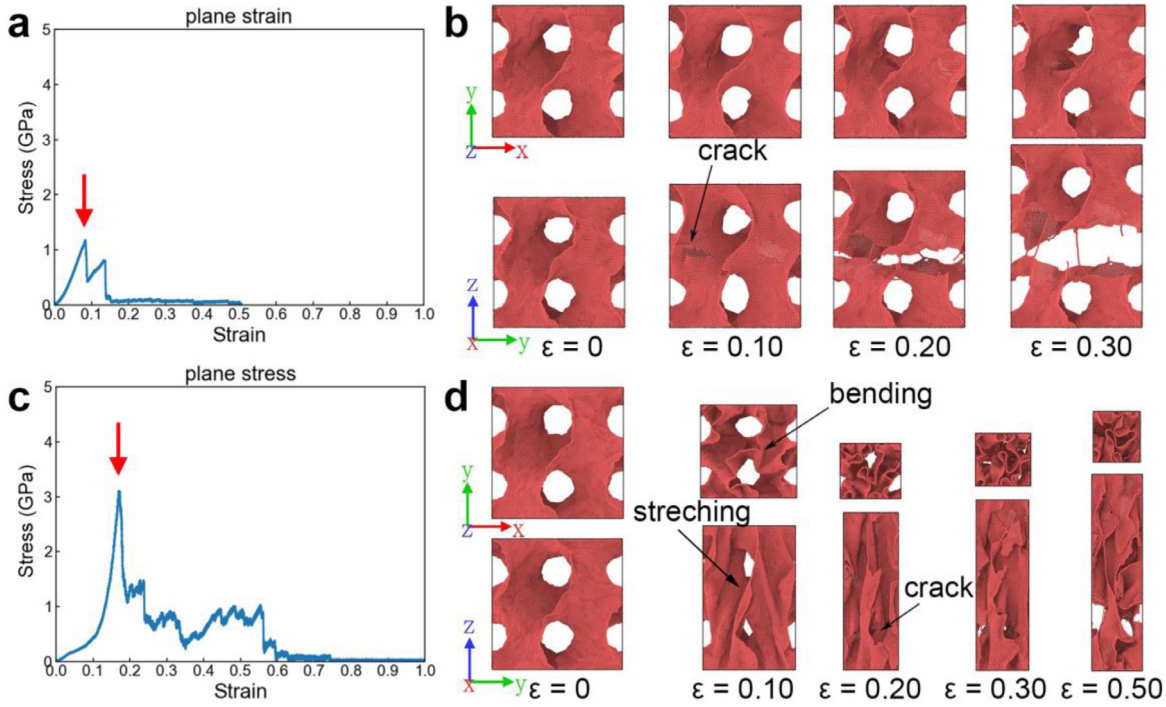

Fig. 4. Tensile stress–strain curves and corresponding snapshots showing the microstructural evolution of a TRD-0.50 graphene gyroid at relative density $\overline{\rho}$ = 0.05; (a, b) plane strain and (c, d) plane stress loading conditions. The red arrow points to the peak tensile stress σ_T in the stress–strain curve. Loading is in the z-direction.

differ in the onset density, i.e., the density at which stiffening commences, attaining a value of 0.1 for 1-layer and 0.2 for 2- and 3-layered gyroids. A similar laterally contraction of the microstructural transformation from bending to stretching happens for the 2-layer graphene gyroid under plane stress as depicted in Fig. S10a and b.

The multilayers reveal no effect on tensile strain ε_T at the peak value of the plane strain and plane stress. Hence, the corresponding tensile strain is only sensitive to the morphology of the structure, dictated by the TRD value. A similar phenomenon of multilayers takes place for TRD-0.10 and TRD-0.25 graphene gyroid materials, as shown in Fig. S11 and Fig. S12.

Tensile behavior of a graphene gyroid: Effect of graphene integrity. Next, we compare the Young's modulus for a gyroid structure with an internal surface area covered by individual randomly deposited graphene sheets of size 1 nm × 1 nm with that consisting of only one continuous graphene sheet as shown in Fig. 7. The one continuous graphene layer is noted to be much stiffer than the multiple random sheets at the same relative density due to the random structure of the graphene ribbons, resulting in pronounced bending contributions and thus featuring a higher density exponent of 0.22 relative to the 1-layer continuous version.

The gyroid graphene of multiple graphene sheets displays a much weaker tensile strength than the one continuous graphene layer, as shown in Fig. 7d and g, and at the same time displays a higher tensile strain ε_T than the one continuous layer case due to the low mechanical integrity of the graphene structure, allowing the structure to accommodate much strain prior to fracture (see Fig. S10c and d). The multiple graphene sheets case also exhibits self-stiffening which happens at a low relative density of 0.075, and at a plateau value close to 0.092 GPa. For both plane strain and plane stress, the σ_T values of the gyroid with multiple graphene ribbons are significantly lower compared to one continuous graphene layer. The tensile fracture strain, on the other hand, is considerably larger for the multiple graphene ribbons, indicating a strong but brittle response for the one continuous layer graphene structures.

Compressive behavior of graphene gyroids. Compressive stress–strain curves of a graphene gyroid depict linear elasticity at low stress values, followed by a long plateau at a constant stress, the collapse stress σ_C. At a certain strain value, a regime of densification is entered, in which the stress rises steeply. Due to the specific morphology of the structures, the bending deformation of the graphene walls dominates the compressive process, as shown in Fig. 8d. The template morphology has a large effect on the compressive strength of graphene gyroids (see Fig. 8a). The TRD-0.10 graphene gyroid exhibits the highest compressive strength under both plane strain and plane stress, contrary to the tensile response shown in Fig. 3. This difference is likely to be caused by the fact that the plate-like structure of the TRD-0.50 samples is more effective in transmitting the load at small strains under tension, while the hollow beam structure of the TRD-0.10 sample is less susceptible to the severe crumpling deformation of the plates at large strains under compression (see Fig. 8d and e). This is consistent with the observation that the exponent in compression of around 2.7 is due to the dominance of bending-dominated behavior during the whole compressive process as depicted in Fig. 8d and e, while in tension there is also a contribution of stretching.

In the case of multilayers, Fig. 8b shows that the stacking of the graphene layers deteriorates the compressive strength of the graphene structure per unit mass, despite the fact that van der Waals force improves the compressive strength compared to the theoretical case of multiple non-interacting layers (compare the solid green and dashed red curve in Fig. 8b). In addition, the multiple graphene ribbons case exhibits a smaller compressive strength per unit mass than the one continuous graphene layer due to the fact that the latter features a continuous covalent connection between the loading points, while for the graphene gyroid with multiple graphene ribbons both covalent and van der Waals interactions dictate the force transmission.

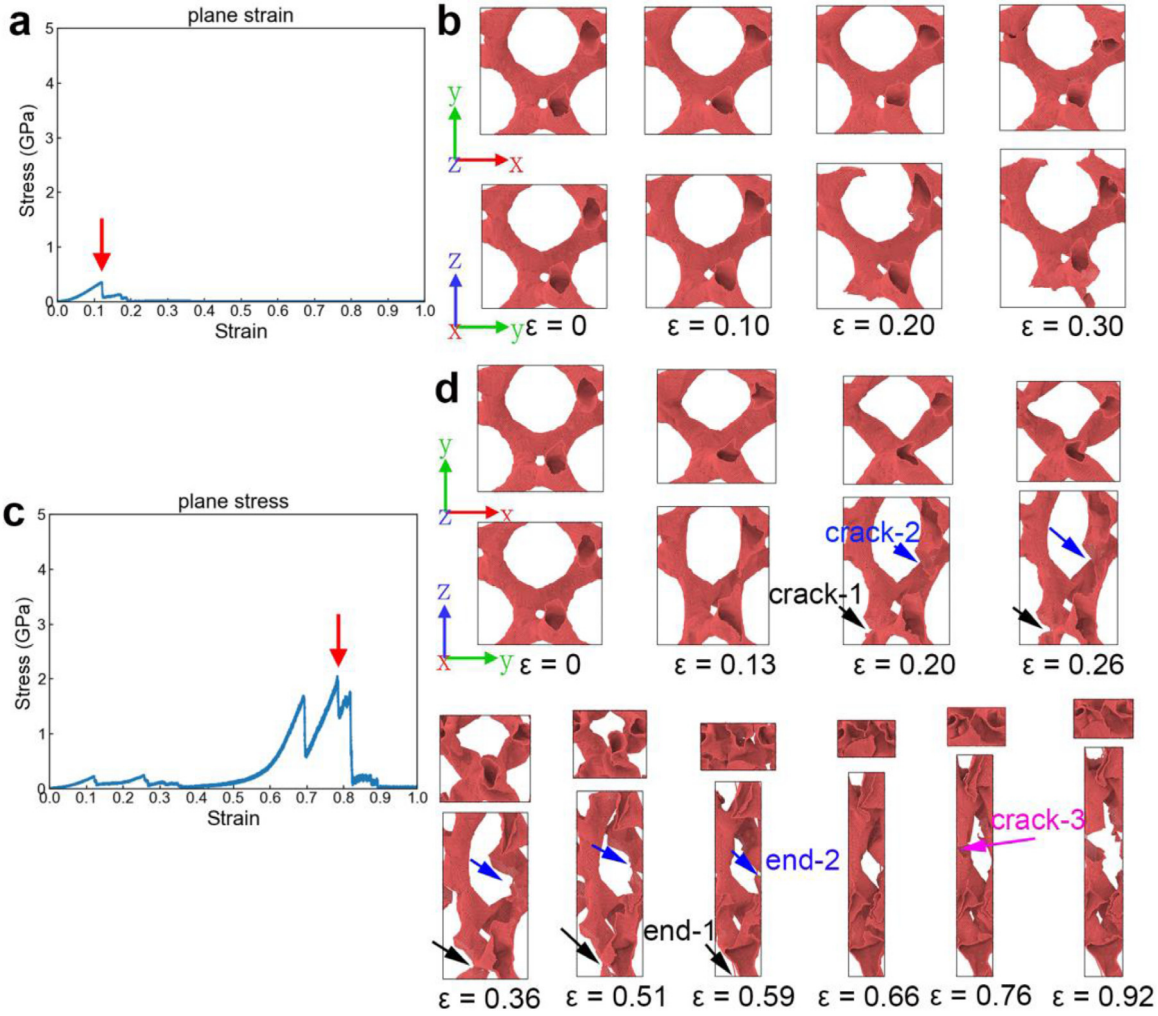

Fig. 5. Tensile stress–strain curves and corresponding snapshots of microstructures evolution of TRD-0.10 graphene gyroid at relative density $\overline{\rho}$ = 0.03. (a, b) plane strain and (c, d) plane stress loading conditions. The red arrow points out the peak tensile stress σ_T in the stress–strain curve. Loading is in the z-direction.

Graphene foams. Fig. 9 depicts the Young's modulus E, tensile strength σ_T, and compressive strength σ_C for three different graphene foam templates featuring one layer of continuous graphene. As can be observed, the Young's modulus, tensile strength and compressive strength are larger for the two regular foams compared to the random foam. Interestingly, the TRD of regular graphene foams does not exhibit a significant impact on the Young's modulus E and tensile strength σ_T. This is probably caused by the fact that changing the template relative density of the regular foam only changes the thickness of the struts and not the topology of the structure, although it has a small effect on the compressive strength σ_C. In addition, only little self-stiffening is observed at a very small relative density in Fig. 9e (TRD-0.20 $\overline{\rho} = 0.05$ and TRD-0.41 $\overline{\rho} = 0.07$).

Finally, the mechanical properties of the nanoporous graphene structures are studied (see Fig. 1c (iv)). In contrast to the other foam structures, the nanoporous graphene structure has a non-periodic unit-cell so that periodic boundary conditions (b.c.) cannot be applied. To allow for a fair comparison, we remove the periodic b.c. of the random foam as well, see Fig. S13. Comparison of the random foam with and without periodic b.c. shows that free edge effects cause the stiffness and strength to be considerably reduced, in line with our previous results [25,51–53]. Next, we compare the random graphene foam with nanoporous graphene (both featuring non-periodic b.c.), showing that the stiffness E and tensile strength σ_T is larger for the random foam at small densities (see Fig. S13a and b). For larger densities (above ∼0.3), however, the opposite is true, resulting in a much larger power-law exponent for nanoporous graphene (4.1 and 3.9 for E and σ_T, respectively) compared to graphene foam (2.7 and 1.3 for E and σ_T, respectively). For the compressive strength σ_c, the nanoporous graphene is stronger for all densities (see Fig. S13c). It is interesting to note that a similar difference in response is also observed for the stiffness of the template structures with the nanoporous gold exponents being of similar value as here (∼4) and much larger than these of the gyroids (∼2) [45].

To summarize the effect of the structural morphology on the mechanical properties of 3D graphene, the Young's modulus E, tensile strength σ_T and compressive strength σ_C of the graphene gyroid, regular graphene foam and random graphene foam are compared in Fig. 10. As can be observed, the Young's modulus and tensile strength are highest for the regular foam and lowest for the random foam, while all three structural morphologies feature bending as the dominant deformation mode, given the power-law scaling exponents of ∼2 and 1.5, respectively. Here, the transition from bending to stretching is especially apparent for the gyroid structures, resulting in the characteristic self-stiffening phenomenon under plane stress conditions (Fig. 10b). It is noted that the exponents in the power law relations differ from other

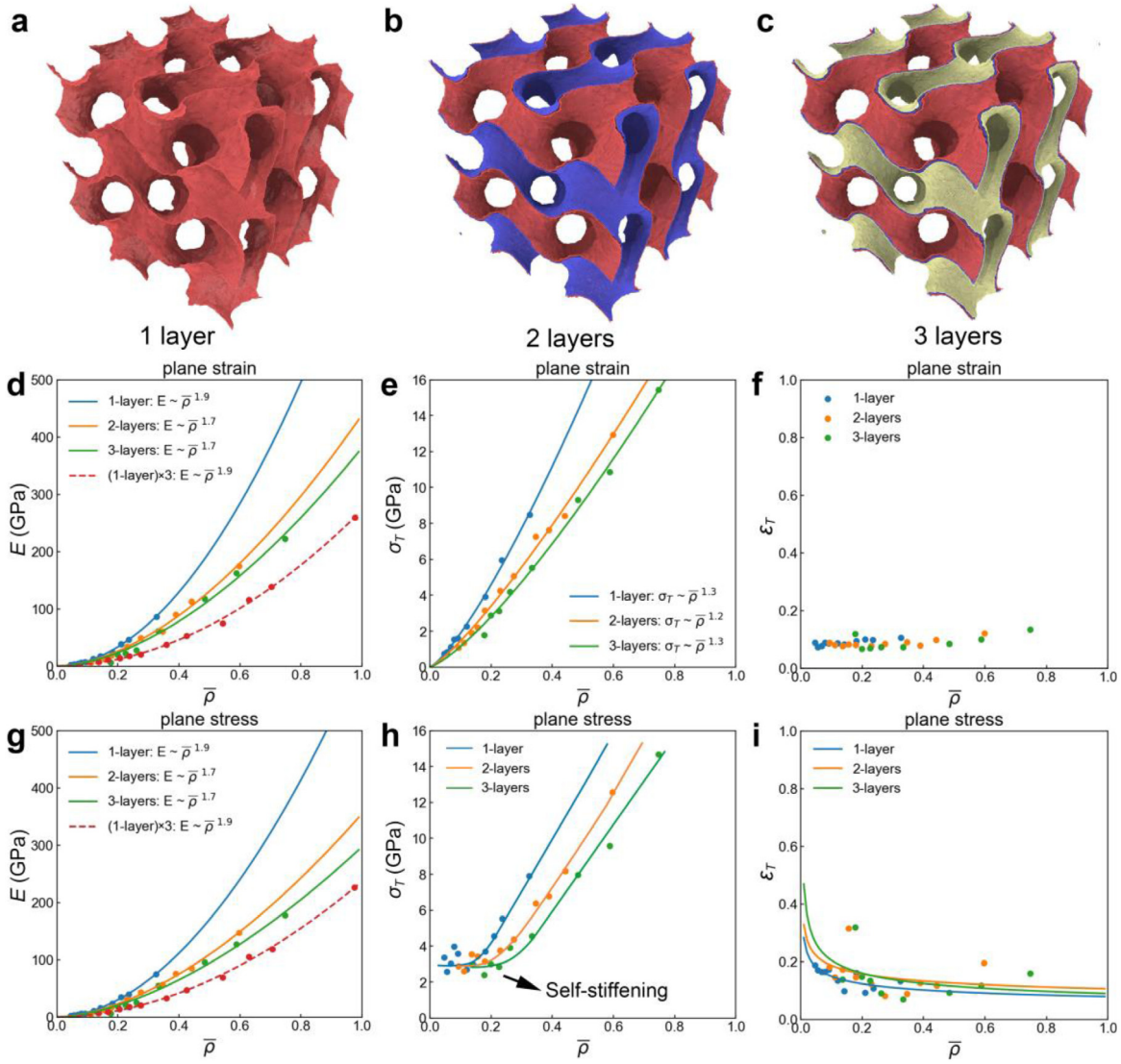

Fig. 6. Effect of the number of graphene layers on the tensile properties of the TRD-0.50 graphene gyroid. (a) 1-layer, (b) 2-layers and (c) 3-layers. Young's modulus E, tensile strength σ_T and tensile strain ε_T of graphene gyroids with 1, 2 or 3 layers under plane strain (d, e, f) and plane stress (g, h, i) loading conditions. The results denoted by '(1-layer)×3' in (d) and (g) corresponds to the case of 3 non-interaction graphene layers, computed by tripling the stiffness and relative density value of the 1-layer graphene sample.

studies [35,41]. This is mainly due to the difference in the structural morphology of the 3D graphene structures. In the two studies, the 3D graphene structures are based on a fully random distribution of graphene sheets, while in our paper we made the 3D graphene with continuous graphene layers. For the compressive strength, the relative ordering is similar as for the stiffness, but with an even larger contribution of bending given the scaling exponents of around 2.5–3.

Conclusions

In summary, we systematically investigated the mechanical properties of 3D graphene structures: graphene gyroids, regular graphene foam, random graphene foam and nanoporous graphene by varying a range of microstructural parameters: the graphene relative density, the template relative density and the number of graphene layers. The Young's modulus, tensile strength, tensile fracture strain and compressive strength as a function of the microstructural parameters are analyzed and compared in detail.

1. We tested samples under plane strain and plane stress conditions, showing a profoundly different response. The gyroid structures show a clear self-stiffening response under plane stress due to a strong reorientation of the gyroid graphene walls in the loading direction for small relative densities. This self-stiffening results in a considerably increased tensile fracture stress and strain which makes the materials both stronger and more ductile, aspects that are important for structural applications. This feature is absent under plane strain and also was not found to occur for the other graphene morphologies (graphene foams and nanoporous graphene).
2. The effect of the number of continuous graphene layers was found to be two-fold; First, the mechanical properties per added graphene layer were found to increase due to the additional van der Waals interactions between layers. On the other hand, adding additional layers makes the material less stiff and strong per unit added mass.
3. We also compared gyroids with one continuous layer to gyroids with multiple cross-linked graphene ribbons. Here,

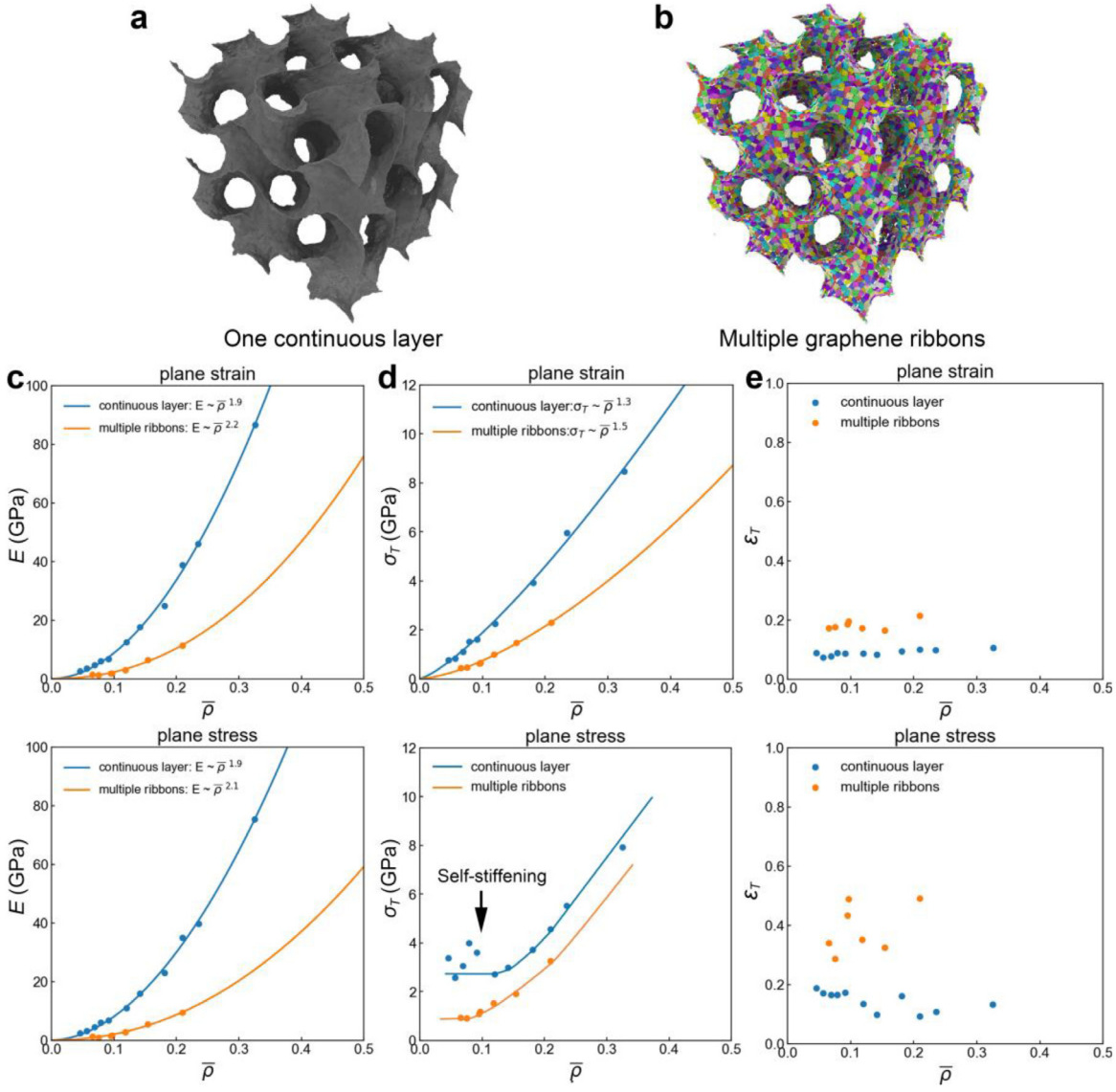

Fig. 7. Comparison of the tensile properties of (a) one continuous layer and (b) multiple graphene ribbons for TRD-0.50 graphene gyroids. Young's modulus E, tensile strength σ_T and tensile strain ε_T of as a function of the graphene relative density $\overline{\rho}$ under (c, d, e) plane strain and (f, g, h) plane stress loading conditions.

the lower number of covalent bonds per unit overall graphene mass leads to additional bending deformations and thus decreases the mechanical properties compared to the gyroids with one continuous layer. On the other hand, the enhanced compliance also increases the ductility which might counter-balance the reduced stiffness in engineering applications.

4. The effect of the template relative density (TRD) was found to strongly affect the microstructural morphology of the resulting graphene gyroid, leading to a stiffer and stronger material, but at the expense of ductility: the tensile failure strain was found to decrease with increasing TRD while the stiffness increased.
5. Finally, we studied the effect of the microstructural architecture of the different 3D graphene structures on the mechanical properties. We found that the stiffness was largest for the regular graphene foams and smallest for the random foams. The scaling exponents for the different architectures was around 1.5 for the tensile strength, around 2 for the stiffness and larger than 2.5 for the compressive strength, showing an increasing contribution of bending to the overall response. The nanoporous graphene was found to have the largest scaling exponent, ranging from 3 for compression to 4 for stiffness and tensile strength, in line with other studies.

Declaration of competing interest

The authors declare that they have no known competing financial interests or personal relationships that could have appeared to influence the work reported in this paper.

Acknowledgments

The present authors are appreciated to the financial support from the National Natural Science Foundations of China (Grant no. 52075417 and 51475359). The present authors are appreciated to the China Scholarship Council (CSC) (No. 201906280167).

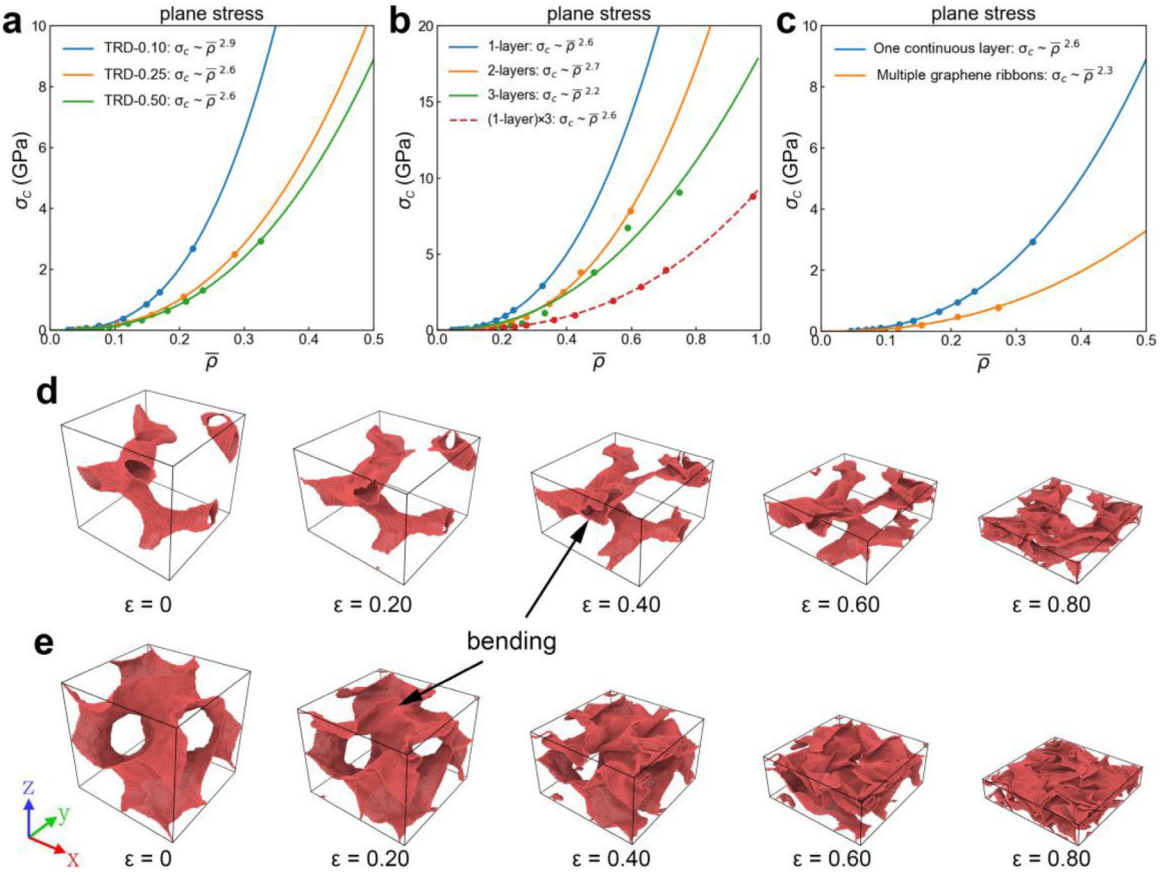

Fig. 8. Compressive strength (σ_C) as a function of relative density $\overline{\rho}$ of graphene gyroid under plane stress. (a) The effect of TRD. (b) The effect of number of graphene layers. (c) The effect of graphene integrity. (d) TRD-0.10 and (e) TRD-0.50 under compressive deformation respectively.

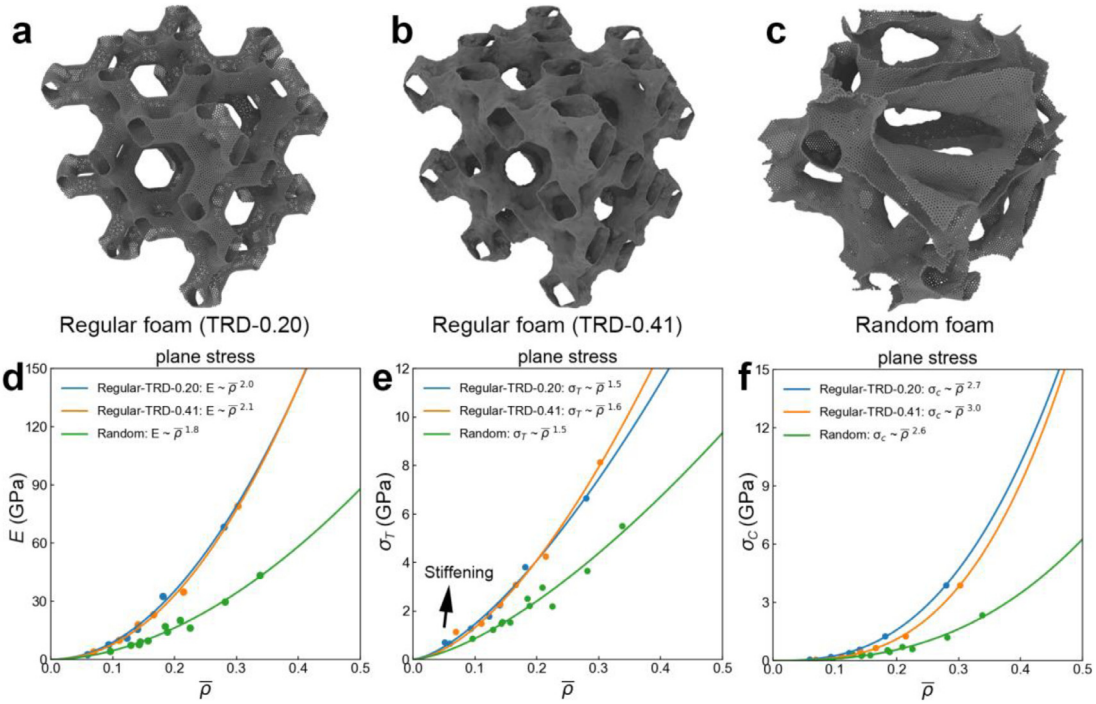

Fig. 9. Mechanical properties of the graphene foams. (a) TRD-0.20 regular graphene foam. (b) TRD-0.41 regular graphene foam. (c) Random graphene foam. (d) Young's modulus E, (e) tensile strength σ_T and (f) compress strength σ_C as function of relative density $\overline{\rho}$ of the different graphene foams loaded under plane stress.

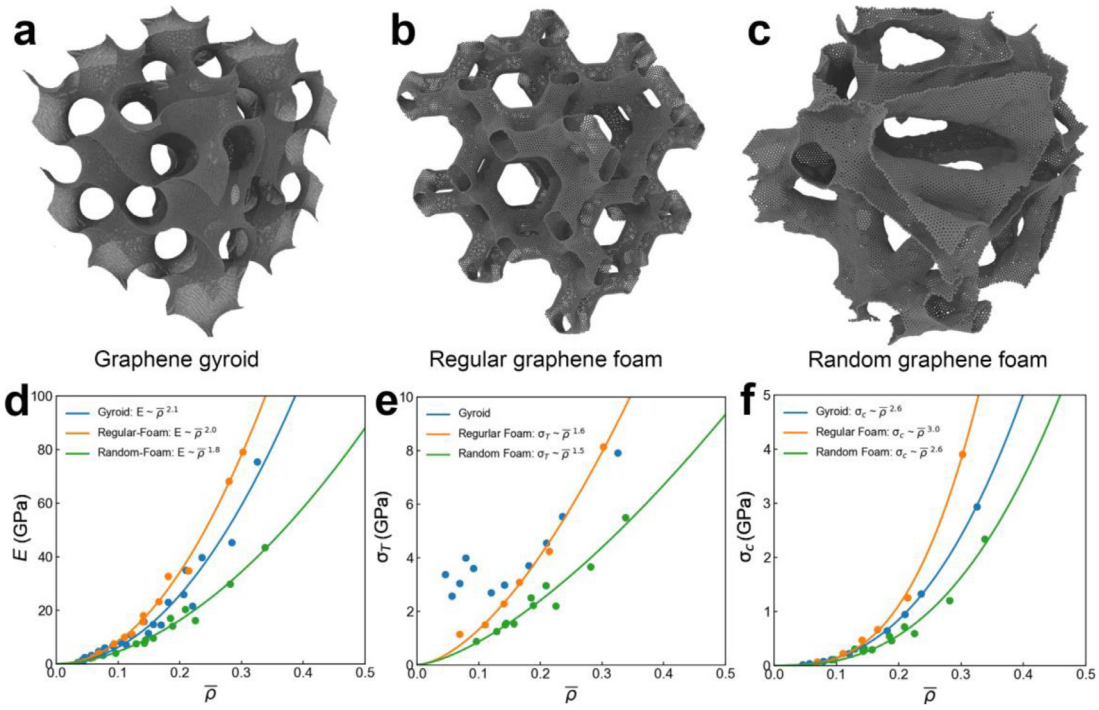

Fig. 10. Summary of mechanical properties for different graphene structures. (a) graphene gyroid, (b) regular graphene foam and (c) random graphene foam. (d) Young's modulus E, (e) tensile strength σ_T and (f) compress strength σ_C as function of relative density $\overline{\rho}$ under plane stress.

Appendix A. Supplementary data

Supplementary material related to this article can be found online at https://doi.org/10.1016/j.eml.2022.101737.

References

[1] A.K. Geim, Graphene: Status and prospects, Science 324 (2009) 1530–1534.
[2] A.K. Geim, K.S. Novoselov, The rise of graphene, Nature Mater. 6 (2007) 183–191.
[3] N.M.R. Peres, The electronic properties of graphene and its bilayer, J. Phys.: Condens. Matter 244 (2010) 4106–4111.
[4] C.L. Pavithra, B.V. Sarada, K.V. Rajulapati, T.N. Rao, G. Sundararajan, A new electrochemical approach for the synthesis of copper-graphene nanocomposite foils with high hardness, Sci. Rep. 4 (2014) 4049.
[5] A.A. Balandin, S. Ghosh, W. Bao, I. Calizo, D. Teweldebrhan, F. Miao, C.N. Lau, Superior thermal conductivity of single-layer graphene, Nano Lett. 8 (2008) 902.
[6] T. Wejrzanowski, M. Grybczuk, M. Chmielewski, K. Pietrzak, K.J. Kurzydlowski, A. Strojny-Nedza, Thermal conductivity of metal-graphene composites, Mater. Des. 99 (2016) 163–173.
[7] L. Changgu, W. Xiaoding, W. K. Jeffrey, H. James, Measurement of the elastic properties and intrinsic strength of monolayer graphene, Science 321 (2008) 385–388.
[8] J.C. Meyer, A.K. Geim, M.I. Katsnelson, K.S. Novoselov, T.J. Booth, S. Roth, The structure of suspended graphene sheets, Nature 446 (2007) 60–63.
[9] Q. Fang, Y. Shen, B. Chen, Synthesis, decoration and properties of three-dimensional graphene-based macrostructures: A review, Chem. Eng. J. 264 (2015) 753–771.
[10] S. Weng, H. Ning, T. Fu, N. Hu, Y. Zhao, C. Huang, X. Peng, Molecular dynamics study of strengthening mechanism of nanolaminated graphene/Cu composites under compression, Sci. Rep. 8 (2018).
[11] J.J. Shang, Q.S. Yang, L. Xia, W. Chao, Compressive deformation mechanism of honeycomb-like graphene aerogels, Carbon 134 (2018) 398–410.
[12] G. Chen, Y. Liu, L. Fei, Z. Xiao, Fabrication of three-dimensional graphene foam with high electrical conductivity and large adsorption capability, Appl. Surf. Sci. 311 (2014) 808–815.
[13] Y. Ma, Y. Chen, Three-dimensional graphene networks: Synthesis, properties and applications, Natl. Sci. Rev. 2 (2015) 40–53.
[14] J. Lavanya, N. Gomathi, Synthesis and characterization of nickel oxide/graphene sheet/graphene ribbon composite, in: National Conference on Thermophysical Properties, 2016, pp. 183–191.
[15] Z. Qi, J. Ye, W. Chen, J. Biener, E.B. Duoss, C.M. Spadaccini, M.A. Worsley, C. Zhu, 3D-printed, superelastic polypyrrole-graphene electrodes with ultrahigh areal capacitance for electrochemical energy storage, Adv. Mater. Technol. 3 (2018) 1800053.
[16] C. Zhu, T.Y. Han, E.B. Duoss, A.M. Golobic, J.D. Kuntz, C.M. Spadaccini, M.A. Worsley, Highly compressible 3D periodic graphene aerogel microlattices, Nature Commun. 6 (2015) 6962.
[17] Q. Zhang, X. Xu, D. Lin, W. Chen, G. Xiong, Y. Yu, T.S. Fisher, H. Li, Hyperbolically patterned 3D graphene metamaterial with negative Poisson's ratio and superelasticity, Adv. Mater. 28 (2016) 2229–2237.
[18] B. Juergen, D. Subho, S. Lihua, W. Di, M.A. Worsley, W. Arne, J.R.I. Lee, M.M. Biener, C.A. Orme, S.O. Kucheyev, Macroscopic 3D nanographene with dynamically tunable bulk properties, Adv. Mater. 24 (2012) 5017.
[19] H. Han, Z. Zongbin, W. Wubo, G. Yury, Q. Jieshan, Ultralight and highly compressible graphene aerogels, Adv. Mater. 25 (2013) 2219–2223.
[20] M.A. Worsley, T.T. Pham, Y. Aiming, S.J. Shin, J.R.I. Lee, B.H. Michael, M. William, Z. Alex, Synthesis and characterization of highly crystalline graphene aerogels, ACS Nano 8 (2014) 11013–11022.
[21] Y. Wu, N. Yi, L. Huang, T. Zhang, S. Fang, H. Chang, N. Li, J. Oh, J.A. Lee, M. Kozlov, Three-dimensionally bonded spongy graphene material with super compressive elasticity and near-zero Poisson's ratio, Nature Commun. 6 (2015) 6141.
[22] F. Zhang, L. Ping, D. Ge, S. He, Fabrication and properties of three-dimensional nanoporous graphene foams with magnesium binder, Scr. Mater. 111 (2016) 89–93.
[23] X. Zhen, S. Haiyan, Z. Xiaoli, G. Chao, Ultrastrong fibers assembled from giant graphene oxide sheets, Adv. Mater. 25 (2013) 188–193.
[24] Z. Chen, W. Ren, L. Gao, B. Liu, S. Pei, H.M. Cheng, Three-dimensional flexible and conductive interconnected graphene networks grown by chemical vapour deposition, Nature Mater. 10 (2011) 424–428.
[25] P.R. Onck, S.S.R. Saane, Atomistic modeling of the stiffness, strength and charge-induced actuation of graphene nanofoams, Extreme Mech. Lett. 5 (2015) 54–61.
[26] H. Bi, I.W. Chen, T. Lin, F. Huang, A new tubular graphene form of a tetrahedrally connected cellular structure, Adv. Mater. 27 (2015) 5943–5949.
[27] X. Xu, Q. Zhang, Y. Yu, W. Chen, H. Hu, H. Li, Naturally dried graphene aerogels with superelasticity and tunable Poisson's ratio, Adv. Mater. 28 (2016) 9223–9230.
[28] X. Zhen, Z. Yuan, L. Peigang, G. Chao, Strong, conductive, lightweight, neat graphene aerogel fibers with aligned pores, ACS Nano 6 (2012) 7103–7113.
[29] W. Chen, L. Yan, In situ self-assembly of mild chemical reduction graphene for three-dimensional architectures, Nanoscale 3 (2011) 3132–3137.

[30] X. Jiang, Y. Ma*, J. Li, Q. Fan, W. Huang*, Self-assembly of reduced graphene oxide into three-dimensional architecture by divalent ion linkage, J. Phys. Chem. C 114 (2010) 22462–22465.
[31] A.I.A. Tomasz Cebo, James A. Dolan, Robert S. Weatherup, Kenichi Nakanishi, Piran R. Kidambi, Giorgio Divitini, Caterina Ducati, Ullrich Steiner, S. Hofmann, Chemical vapour deposition of freestanding sub-60 nm graphene gyroids, Appl. Phys. Lett. 111 (2017) 253103.
[32] A.E. Garcia, C.S. Wang, R.N. Sanderson, K.M. McDevitt, Y. Zhang, L. Valdevit, D.R. Mumm, A. Mohraz, R. Ragan, Scalable synthesis of gyroid-inspired freestanding three-dimensional graphene architectures, Nanoscale Adv. 1 (2019) 3870–3882.
[33] Y.I. Hamzeh Kashani, Jiuhui Han, Pan Liu, Mingwei Chen, Extraordinary tensile strength and ductility of scalable nanoporous graphene, Sci. Adv. 5 (2019) eaat695.
[34] C. Wang, C. Zhang, S. Chen, The microscopic deformation mechanism of 3D graphene foam materials under uniaxial compression, Carbon 109 (2016) 666–672.
[35] D. Pan, C. Wang, T.C. Wang, Y. Yao, Graphene foam: Uniaxial tension behavior and fracture mode based on a mesoscopic model, ACS Nano 11 (2017) 8988–8997.
[36] F. Meng, C. Chen, D. Hu, J. Song, Deformation behaviors of three-dimensional graphene honeycombs under out-of-plane compression: Atomistic simulations and predictive modeling, J. Mech. Phys. Solids 109 (2017) 241–251.
[37] Z. Zhang, A. Kutana, Y. Yang, N.V. Krainyukova, E.S. Penev, B.I. Yakobson, Nanomechanics of carbon honeycomb cellular structures, Carbon 113 (2017) 26–32.
[38] J.J. Shang, Q.-S. Yang, X. Liu, C. Wang, Compressive deformation mechanism of honeycomb-like graphene aerogels, Carbon 134 (2018) 398–410.
[39] L. Yi, T. Chang, X.-Q. Feng, Y. Zhang, J. Wang, B. Huang, Giant energy absorption capacity of graphene-based carbon honeycombs, Carbon 118 (2017) 348–357.
[40] G.S. Jung, M.J. Buehler, Multiscale mechanics of triply periodic minimal surfaces of three-dimensional graphene foams, Nano Lett. 18 (2018) 4845–4853.
[41] G.S.J. Zhao Qin, Min Jeong Kang, Markus J. Buehler, The mechanics and design of a lightweight three-dimensional graphene assembly, Sci. Adv. 3 (2017) e1601536.
[42] Y. Jung, S. Torquato, Fluid permeabilities of triply periodic minimal surfaces, Phys. Rev. E 72 (2005) 056319.
[43] W.-Y. Jang, A.M. Kraynik, S. Kyriakides, On the microstructure of open-cell foams and its effect on elastic properties, Int. J. Solids Struct. 45 (2008) 1845–1875.
[44] X.-B. Wang, X.-F. Jiang, Y. Bando, Blowing route towards advanced inorganic foams, Bull. Chem. Soc. Jpn. 92 (2019) 245–263.
[45] S.S.R. Saane, K.R. Mangipudi, K.U. Loos, J.T.M. De Hosson, P.R. Onck, Multiscale modeling of charge-induced deformation of nanoporous gold structures, J. Mech. Phys. Solids 66 (2014) 1–15.
[46] S.J. Stuart, A.B. Tutein, J.A. Harrison, A reactive potential for hydrocarbons with intermolecular interactions, J. Chem. Phys. 112 (2000) 6472.
[47] T. Zhang, X. Li, S. Kadkhodaei, H. Gao, Flaw insensitive fracture in nanocrystalline graphene, Nano Lett. 12 (2012) 4605–4610.
[48] A. Pedrielli, S. Taioli, G. Garberoglio, N.M. Pugno, Designing graphene based nanofoams with nonlinear auxetic and anisotropic mechanical properties under tension or compression, Carbon 111 (2017) 796–806.
[49] F. Liu, R. Zou, N. Hu, H. Ning, C. Yan, Y. Liu, L. Wu, F. Mo, Understanding the mechanical properties and deformation behavior of 3-D graphene-carbon nanotube structures, Mater. Des. 160 (2018) 377–383.
[50] A. Stukowski, Visualization and analysis of atomistic simulation data with OVITO–the open visualization tool, Modelling Simulation Mater. Sci. Eng. 18 (2010) 015012.
[51] C. Tekoglu, P. Onck, Size effects in two-dimensional Voronoi foams: A comparison between generalized continua and discrete models, J. Mech. Phys. Solids 56 (2008) 3541–3564.
[52] E.W. Andrews, G. Gioux, P. Onck, L.J. Gibson, Size effects in ductile cellular solids. Part II: Experimental results, Int. J. Mech. Sci. 43 (2001) 701–713.
[53] P.R. Onck, E.W. Andrews, L.J. Gibson, Size effects in ductile cellular solids. Part I: Modeling, Int. J. Mech. Sci. 43 (2001) 681–699.